Research report

Magnetic filaments: State of the art

Mostarac, MSc
Faculty of Physics, Universiy in Vienna
10.Feb.2020

1   Current state of research and own research goals

Stimuli-responsive materials are one of the central research topics in modern soft mater physics.[1, 2] Responsiveness to magnetic fields proves is particularly tantalising, due to the dynamic control of their intensity, great spatial resolution achievable with them, and the fact that magnetic fields do not interfere with biological tissues and processes.[3] Therein came the idea that different classes of soft matter could be combined with magnetic nanoparticles (MNPs), creating a new class of magnetic soft mater. By MNPs, one refers either to ferromagnetic or super-paramagnetic ones.[4] In the case where micron sized, multi-domain particles are used, one has to distinguish between magnetically soft and hard MNPs.[5] Overarching framework and the point of interest of our research as it pertains to magnetic soft matter are magnetic filaments (MFs).[6, 7] MFs can largely be considered analogous to polymer chains (though at a supracolloidal scale) where the MNPs serve as polymer monomers and the crosslinkers play the part of chemical bonds between them. One can divide available MF systems base on two criteria: type of magnetic monomers (super-paramagnetic or ferromagnetic), and/or rigidity. Discrimination based on rigidity is basically equivalent to distinguishing filament systems based on crosslinking. Despite the substantial amount of publications on theoretical an computational modeling,[8–28] and synthesis methods of such systems (which grew to be rather diverse),[6, 7, 29–44, 44–54] flexible, nanoscale MFs, which have a finely controllable micro-structure, remain to be experimentally realized. However, contemporary synthesis techniques, such as the ones based on programmable DNA-MNP assembly show promise on route towards synthesis of MFs with desirable magneto-mechanical properties.[55–61] An assembly mechanism where the structure building instructions are embedded within a pre-defined set of different DNA-framed nanoparticles (NPs), along with DNA polyhedral frames, enables designing diverse planar constructs, 1D, 2D and 3D frameworks.

2   Design Criteria

We have invested significant time and energy in exploring the range of potential benefits that these systems could have over systems that are achieved with traditional synthesis approaches, by computational modeling and MD simulations. Let us quantify the benefits that magnetic filaments as we define them, have over similar materials, by contrasting the magnetic responses of such systems. Commonly used theoretical descriptions of magnetization of soft mater systems are the Langevin magnetization law, and mean filed approaches, such as MMFT2.[62] For non-interacting monomers, corresponding field dependence of normalized magnetization along the field direction would follow the Langevin function. If the assumption that dipolar forces do not lead to cluster formation, the effect of the additional dipole-dipole interactions, and hence an additional dipole field to the external magnetic field, can be accounted for by an effective, homogeneous net field.[63] For this assumption, MMFT2 faithfully represents static magnetic properties of relatively concentrated ferrofluids. The defining characteristics of what we call a magnetic filament are as follows:

- Magnetic monomers are permanently crosslinked by means of macromolecules, which constitutes what we refer to as a backbone

- There is well defined relationship between the crosslinking and the orientations of the dipole moments of the monomers, where it is a design choice if one wants to fully couple or decouple their rotational degrees of freedom.

- Magnetic properties on the filament level are entirely determined by the properties of individual monomers, and the microstrucure defined by the placement of NPs within the backbone.

- When a filament is fully stretched, magnetic monomers within the conformation necessarily lie on a single line.

- Monomers within a filament can be either ferromagnetic or super-paramagnetic. In the later case, we use our own procedure to account for magnetization effects, explicitly, and accounting for no-linear effects.

Our first order approximation coarse-grained model, refereed to throughout this report as the generalised crosslinking model, that fulfills all of the aforementioned criteria, is explained in more detail in Appendix A. Here we just highlight the key features as follows:

- monomers are modelled as soft core spheres, with accurate representation of the magnetic nature of both ferromagnetic and super-paramagnetic monomers, interacting via the dipole-dipole potential.

- for super-paramagnetic properties we account for nonlinear magnetisation effects explicitly

- crosslinking of ferromagnetic monomers covers two possibilities. For NPs, connecting potential springs can be attached either to the centers of NPs, allowing free rotation of the NPs irrespective of the backbone (plain crosslinking), or they are connected to anchoring points on NPs, with permanent positions correspond to the orientation of the dipole moments, therefore coupling the orientations of the backbone and the MNPs (constrained crosslinking).

- crosslinking of super-paramagnetic monomers covers two possibilities. For NPs, connecting potential springs can be attached to the centers of NPs with an additional bending potential, that allows us to tune the rigidity of the backbone (constrained crosslinking), or without a bending potential (plain crosslinking)

It turns out that MMFT2 describes the magnetisation of MFs well, only for plain crosslinking and weekly magnetic monomers. For all other parameter sets we explored, the crosslinking enhances the magnetisation, and MFs outperform conventional ferrofluids by a significant margin (up to 30% higher magnetisation in some cases). Given a choice of a particular MNP, i.e. magnetite nanoparticles coated with oleic acid coating, 2nm thick, with MNPs with size of 10 nm, the saturation magnetisation values correspond to dipole moments of $2.51 x 10^{-19} \ Am^2$. This also means that the maximum of the applied magnetic field range represents relatively modestly strong fields of only $0.11 \ T$. Such NPs are super-paramagnetic, and despite them being weakly magnetic, in a crosslinking scenario such as constrained crosslinking, as depicted in Fig.1(c), they outperform conventional ferrofluids in terms of magnetisation by 10%, in external magnetic filed of about 0.04 T. Based on investigations using the generalised crosslinking model, we discerned several key design points to pay attention to and try to uphold. For details about crosslinking models used here, along with detailed descriptions of the generalised crosslinking model, we refer the reader to Appendix A. In no particular order, these are the design criteria that we went in with, as we attempted to synthesise MFs using DNA origami technology, as guest in Prof. Gangs research groups at Columbia University (CUNY) and Brookhaven National Laboratories (BNL):
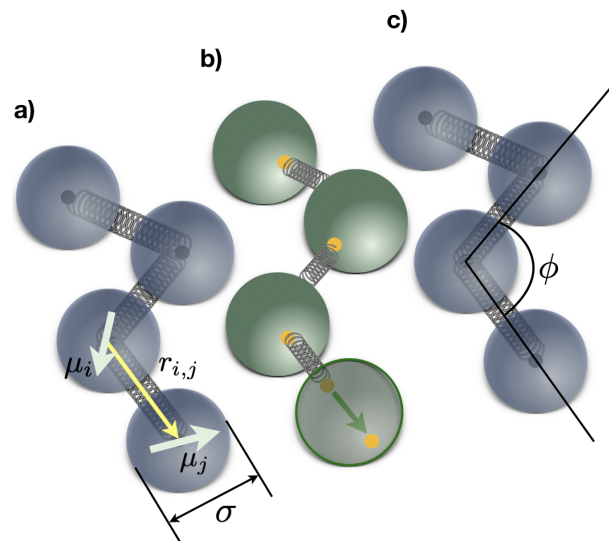

Figure 1: Schematic representations of three crosslinking mechanisms. Detailed explanations can be found in Appendix A. Dipole moments are depicted as arrows. The connectivity mechanisms are depicted as springs attached to either filament centres (black dots) or to anchoring sites with permanently fixed positions on the surface of MNPs (yellow dots).(a) Plain crosslinking model; (b) Constrained crosslinking model for ferromagnetic MNPs; (c) Constrained crosslinking model for super-paramagnetic MNPs.

- The most important distinguishing factor between MFs, is not the magnetic nature of the monomers, but rather the crosslinking approach. This can easily be depicted if we mention the fact that in terms of magnetisation, ferromagnetic monomers in plain crosslinking scenarios, such as depicted in Fig.1(a), behave the same as super-paramagnetic ones. Furthermore, in the presence of central attraction between the monomers (which is not an unreasonable presupposition for DNA origami based systems), there is a parameter region for which super-paramagnetic MFs with plain crosslinking an central attraction, exhibit an explicit bimodal energy distribution, which might be an indication of a critical point, similarly to the case of Stockmayer filaments with ferromagnetic monomers, and in fact suggests that super-paramagnetic monomers inside such MFs behave similarly to ferromagnetic monomers in Stockmayer fluids.

- Furthermore, in terms of overall magnetization, super-paramagnetic monomers can actually dominate ferromagnetic ones, when put in constrained crosslinking scenarios, as depicted in Fig1.2(b) and (c), respectively, for strongly magnetic monomers. Of course, the magnetic response of the filaments is capped by the degree to which the dipole moments in a filament can conform to a head-to-tail arrangement. It is therefore important to make sure that the monomers truly form assembly's that are as linear as possible, as not to inhibit their ability to minimize their magnetic energy.

- For ferromagnetic monomers , it is preferable to have a crosslinking that fully couples the relative rotations of the monomers to the filament backbone, akin to what is depicted in Fig.1(b), and make sure that dipole moments of the monomers are aligned as much as possible along the filament backbone.

- For super-paramagnetic monomers however, backbone rigidity proves to be the discerning factor, particularly resistance of the backbone to bending. Increase rigidity of the backbone can lead to enhanced magnetic response of super-paramagnetic monomers, even when compared to ferromagnetic ones, while also reducing the bending tendencies that super-paramagnetic filaments have. Namely, instead of reorientation of the filament as a whole, as directed by the external magnetic filed applied, super-paramagnetic filaments bend the backbone and fold in order to minimise free energy.

- Topological impurities are a matter of concern and significantly impede magnetic properties of MFs. The key measure to pay attention to here is the average inter-particle distance. It is therefore advantageous to consider crosslinking MNPs in a way that will have the average inter-particle distance on the order of colloid diameter. Furthermore, in situations where one impregnates the pre-assembled backbone, as suggested we will have done, it is important to make sure that the "filling" yield is high.

- when not subjected to an external magnetic field, MFs should ideally, in its polymeric properties resemble (as closely as possible) a real polymer. Once subjected to an external magnetic field, one should be able to manipulate several properties such as induce a sense of orientation, modify the radius of gyration and/or stiffens of such chain-like conformations. We have found that super-paramagnetic MFs with constrained crosslinking have a more on/off kind of reaction to external magnetic fields, compared to ferromagnetic ones, where end-to-end distance increase with field is more progressive.

- Ferromagnetic and super-paramagnetic MFs with plain crosslinking have tendencies to fold, into thermodynamically stable configurations. Therefore, they should treated as a separate class, as they advantages are in depicted in different place, rather than field induced stretching and magnetisation mechanism.

3   Synthesis of Experimental Systems

The strategy for the designed fabrication of magnetic nanoparticle filaments is based on programmable DNA-NP assembly.[57, 64–67] The principal aim of this novel technique is to create individual DNA-NP complexes with well-defined and prescribed binding sites. Such an approach, relies on placing the NPs inside DNA cage-like structures, leveraging the benefits of anisotropic, selective interaction sites. Using DNA origami technology, one can fabricate cages of various geometries and sizes, with specifically designed, fully controllable (by means of DNA sequence encoding) binding vertices.[67] These vertices,

fully determine the self-assembly structure of the cages, and finally, the geometry of the possible superstructures that the cages can hybridize into.[61, 68] Furthermore, NPs can be functionalized with complementary single-stranded DNA, which can be localized and crosslinked to the cage structure via DNA hybridization.

Shifting the assembly from the NPs to the DNA origami frames, allows us to use an approach that is in spirit akin to patchy particles. Leveraging of anisotropic interaction potentials, and selective bonding would be impossible if MNPs were left to their own devices. By defining the positions of NPs by creating an origami backbone aforehand, one effectively splits the synthesis process in to two phases.

- First phase entails satisfying our design criteria on the level of the NPs functionalization, where magnetic properties on the level of a single colloid are defined by choice of material, diameter of the NPs and NP coating.

- Secondly, by choosing a specific DNA origami structure, one defines the crosslinking and therefore rigidity, on the level of DNA origami assembly, where the versatility and modularity inherent to this approach, allows for remarkable control of the micro-structure. One effectively relegates the chemical and structural stability of NP aggregates to the origami.

Most existing crosslinking procedures for synthesis of such 1D conformations of magnetic NPs are anyway based on the functionalization of MNP surface. In these approaches, one aims that functionalized MNPs assemble between themselves. We advocate however, an approach where MNPs assemble with steric casings in form of DNA origami cages. As already mentioned above, the idea is to have functionalized MNPs, which in this case means that we chemically graft *ssDNA* to the surface of the MNPs. On the other hand, DNA origami casings are designed to have binding sites, that are groups of specific *ssDNA* strands, encoded and positioned so that they will by design, hybridize only with *ssDNA* that is on the surface of functionalized MNPs. These binding sites are to be distinguished from the vertices DNA origami casings also have, which are designed to encode a specific self-assembly behaviour, between the origami casings themselves.

3.1   First Phase

The first phase, as as described above, was explored and settled in preparation for our appointment in Prof. Gangs research groups at CUNY and BNL. As suggested in the design criteria presented in Section 2, given that we have strongly magnetic monomers and that we would want to have a crosslinking that could be placed withing the constrained crosslinking framework, using super-paramagnetic MNPs was preferable. Regardless of our design criteria, using super-paramagnetic particles comes with some practical advantages. Firstly, based on availability, most labs have access to magnetite MNPs. Magnetite MNPs are super-paramagnetic up to 20nm in diameter. Regardless of which DNA origami structure we finally use for synthesis of the backbone, there are bound to be limitation on the size of either the MNP binding sites, on the origami, or geometric limitations to how MNPs can approach these sites. Having this in mind, by using smaller MNPs, one increases the phasespace of possibilities in which the MNPs in fact manage to approach/enter the origami and bond to it, before aggregation becomes a factor. Second big advantage using super-paramagnetic MNPs gave us compared to if we were dealing with ferromagnetic ones, is that we did not need to control the dipole moment orientation of the MNPs w.r.t the origami backbone. This really is one of the biggest advantages that MFs consisting of super-paramagnetic monomers have. It is of paramount importance for the magnetic response of ferromagnetic MFs, to have the dipole moments of the MNPs oriented along the filament backbone axis, whereas super-paramagnetic MFs have no such limitations, as long as the favoured head-to-tail dipole configuration is not physically limited by the crosslinking (hence one of our defining characteristic of MFs being that when MFs are fully stretched, magnetic monomers within the conformation necessarily lie on a single line). Based on a multitude of parallel projects that are also based on on MNP-DNA origami assembly, but are independent from our project, that are run within the research groups of Prof. Gang, we narrowed our choices to the following:

- streptavidin-coated magnetite MNPs with sizes of 20 and 30 nm in diameter, dispersed in PBS buffer

- carboxylic acid-stabilized magnetite MNPs with size of 10 and 15 nm, dispersed in water

- oleic acid-stabilized magnetite MNPs with sizes of 10 and 20 nm, dispersed in toluene

The major issue is low grafting density of *ssDNA* strands on the surface of the particles. However, experience has shown, that for the choice of streptavidin-coated, 20nm magnetite MNPs, we can expect a reasonable surface grafting density, DNA Origami-MNP filling yield, at a reasonable timescale. In principle, given enough time, one should obtain a perfect filling yield. In practice however, because of competing timescales, where MNPs aggregate among themselves, simply waiting longer is not an option. Therefore, we chose to in fact use the streptavidin-coated 20nm magnetite MNPs, given that they are strongly magnetisable, chemically stable and have a solid grafting yield of *ssDNA*.

3.2 Second Phase

Realisation of the second phase of our research, as distinguished above, proved to be much more involved. At the very basic level, we had to deal with a case of "spoiled for choice". DNA origami technology is a well-established approach for fabricating elaborate nanostructures, where a very long scaffold strand folds with hundreds of short staple strands to assemble shape-confined DNA architectures. As part of DNA origami technology, modularity and versatility inherent to the approach, mean that we can access a multitude of geometries and ways in which these origami can assemble. However, given that assembling 1D chains out of origami, that fulfill our design criteria, is not something that has been done before, it was not fully clear which one, out of the origami designs that Prof. Gang and his research groups have developed over the years, would be preferable. More importantly though, as was stated in Section 2, crosslinking differentiates MFs more so than the actual magnetic nature of the monomers. In terms of our synthesis approach, choosing a specific DNA origami structure is equivalent to defining a crosslinking approach. Furthermore, when choosing the origami system, we had to be aware that each one them entails their own set of difficulties as it pertains to experimental measurements. In any case, we attempted to synthesise 1D chains of DNA origami casings with the Hollow Square origami, a choice which we present and justify in detail below.

3.2.1 Hollow Square

We used the so-called Hollow Square origami (HSo) structures, designed as $28 \times 28 \times 28$ nm hollow cube with a $20 \times 20 \times 28$ nm cuboid cavity (Fig.2(a)). The hollow square origami, is formed with two-layer double helix wall (outer layer: 12×12 double helix, inner layer: double 10×10 helix). Key features of this DNA origami are that the inner cavity can encapsulate functionalized NPs and the outer DNA wall can be encoded to independently guide binding interactions in three orthogonal directions. HSo is designed so that they have programmed groupings of *ssDNA* as can be seen on Fig.2(b), which allow them to assemble between one another, and build 1D chains, where we can also encode a relative orientation between the assembled HSo. Furthermore, we can design additional external binding sites, as depicted in Fig.2(c), or internal binding sites, as depicted in Fig.3(d), made so that they will hybridize only with *ssDNA* on the surface of functionalized NPs that we want to create Origami-NP complexes with.
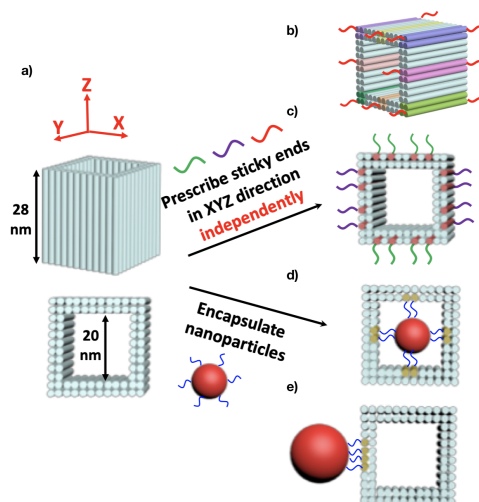

Figure 2: schematic depiction of hollow square origami, DNA origami steric casings, designed for assembly of 1D chain conformations, and meant to encode binding sites for MNPs.

Given that we chose to use 20nm NPs, it is was unclear whether we would be able to successfully bind them to the origami if the binding sites were inside the cuboid cavity. Based on dimensions of both the sides of the hollow cavity and of the NPs, surely they can fit inside. But whether they would be able to diffuse inside the cavity with a reasonable frequency and how high could the yield be, before we start having significant problems with NP aggregation was unclear. Therefore, we opted for an alternative approach where the binding vertices were put on one of the sides of HSo instead of inside the cuboid cavity. These vertices would eventually be filled with MNPs, as depicted in Fig.2(e). The assembly of 1D chains of DNA origami HSo can be achieved by designing two types of DNA

origami, which are meant to be distinguished by colour in Fig.3. We discern HSo of *Type A*, depicted with binding vertices made out of red colored *ssDNA*, and *Type B* HSo, depicted with binding vertices consisting of blue colored *ssDNA*, respectively. *Type A* HSo would have binding vertices with a particular groupings of *ssDNA* (we distinguish *Z8*, *Z16*, *Z32* in Fig.3), with particular, carefully designed *ssDNA* sequencing. *Type B* HSo would have corresponding groupings of *ssDNA*, with complementary sequencing. Therefore, through DNA base-pairing, the two complementary DNA origami types will bind to each other $-A-B-A-B-$, via the so-called binding vertices, to grow a hierarchical chain in one dimension. It is important to note that not all bases in the *ssDNA* strands are meant to be binding. In actuality, only the last eight bases of a strand of *ssDNA* are designed to be bonded with bases on a complementary type HSo. The rest of the bases within a strand of *ssDNA* are just consequent instances of the nucleobase Tymine, therefore considered as "spacers", and henceforth referred to as poly-T spacers. By modifying the poly-T spacer number, we can modifying the length of the *ssDNA* links.
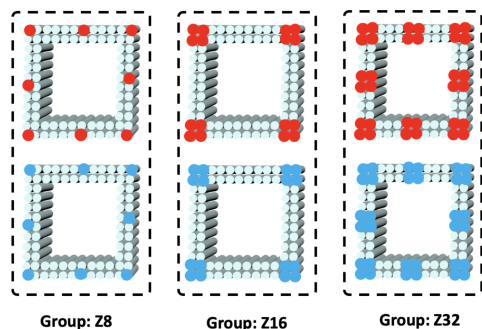

Figure 3: schematic depiction of three designs with different locations of sticky ends along z direction, for hollow square origami design.

In order to understand how effectively we can influence the length of the HSo 1D chains we can assemble, and their rigidity, we explored the effects of changing the number of *ssDNA* inter-cube links and the number of polyT spacers. These two variables determine the bonding energy between two HSos, and are a part of a larger relationship between the chain rigidity and net bonding energy

For the purposes of understanding the effects of changing the number of *ssDNA* inter-cube links, we have made three HSo designs with different locations of sticky ends along z direction (*Z8*, *Z16*, *Z32* in Fig.3). Increasing the number of *ssDNA* complementary strands affects the binding energy between two complementary DNA origami and is expected to affect chain growth. Furthermore, given that for our purposes HSo themselves, are essentially stiff, any flexibility we observe will be a function of *ssDNA* properties, their number, grouping and length. For the design of *Z8*, eight *ssDNA* strands are positioned at the four corners the centres of four sides of the helix wall, respectively. For the design of *Z16*, each corner contains four *ssDNA* strands. For the design of

Z32, each helix corner or centre contains four *ssDNA* strands. For the control of spacer length of binding bonds, we designed a special poly-T sequence to bridge DNA staple part (used for the folding of the origami) and sticky end (the eight nucleobases designed to bond with the ones from *ssDNA* on the correspond type HSo). As previously suggested, the poly-Ts work as spacers, to provide enough freedom of the sticky end for enhancing binding possibility. Hence, by changing the length of this sequence, the flexibility of 1D chain as well as binding efficiency can be tuned. We provided three designs for the spacer control: 20-base poly-Ts, 30-base poly-Ts and 40-base poly-Ts. Taking one DNA strand with staple part and sticky end as an example, the sequences with different functions are shown below (red- sticky end, blue- 30 base poly-T spacer, violet- staple part):

TCCATAGGTTTTTTTTTTTTTTTTTTTTTTTTTTTTTTTTTTGAGTAACATTCTGATTAT

Here, the red sequence binds to a complementary strand, forming binding bonds. Blue sequence is the spacer that offers flexibility. Violet sequence is designed as a staple contributing to origami folding.

3.2.1.1 TEM Imaging   In Figs. 4 and 5, we present the extent of different samples we did TEM imaging on, as we were trying to exhaust the parameter space consisting of number of links between two HSos, and poly-T spacer length. Note that time constrains did not allow for us to quantify all of our initial impressions, based on TEM images. Some decisions had to be made on the basis of visual inspection. At this point, we introduce notation where we concatenate the indications for the grouping type (i.e *Z8*) and length of poly-T spacer with a dash, i.e a HSo with 4 linkers per corner and length 20 of poly-T spacer is denoted by *Z16-20*. Looking at Fig 4, one can see that irrespective of the linker groupings (*Z8*, *Z16*, *Z32*), all samples appeared to be rather rigid. However, based on TEM images, we concluded that *Z8-20* HSo are unable to assemble in to chains that are long enough to be of interest. Saying that an assembled 1D chain of HSo is of interest to us entails that the chain has to at least be long enough, so it is reasonable to expect it to be longer that its persistence length. This is a necessary condition if one was
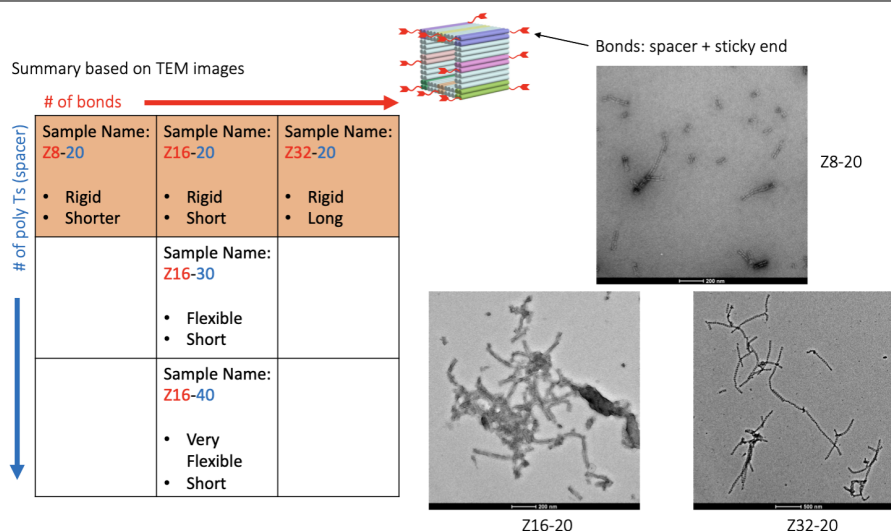
Figure 4: ummary of TEM imaging results for 1D HSo chains, based on changing the number and grouping (*Z8-20*, *Z16-20* and *Z32-20*) of ssDNA linkers.

to speculate about the polymeric properties of such 1D chain conformations of HSo. For chains made out of *Z8-20* HSo, this was not the case. On the other hand, *Z32-20* HSo chains can grow to rather impressive lengths, with a median length of about 60 units per chain. They seem to still be rather stiff, based on TEM imaging. Chains based on *Z16-20* HSo design, while still a bit on the short side of what we would like to have seen, were a significant step up in median number of units per chain (ca. 13 units per chain). Furthermore, given that *Z32-20* HSo based chains looked too stiff, based on visual inspection of TEM images, and having in mind the increase in cost when ordering poly-T spacers for *Z32* Hollow Sqaures compared to *Z16* ones, *Z16-20* HSo were determined the design we should proceed to explore further. *Z16-20* HSo was the reasonable choice, and the design where we could hope to achieve a good compromise between rigidity and length.

Looking at Fig 5, one can see, based on TEM imaging, that the length of poly-T spacers for *Z16* HSo, affects the rigidity of the assembled chains. Furthermore, we expected that increasing the poly-T spacer length would also increase the length of the assembled chains. Even though there is an increase, it is not significant enough to make a real difference for our purposes. Both *Z16-30* & *Z16-40* HSo assemble in chains that are noticeably more flexible then the ones assembled from *Z16-20* HSo. However, the
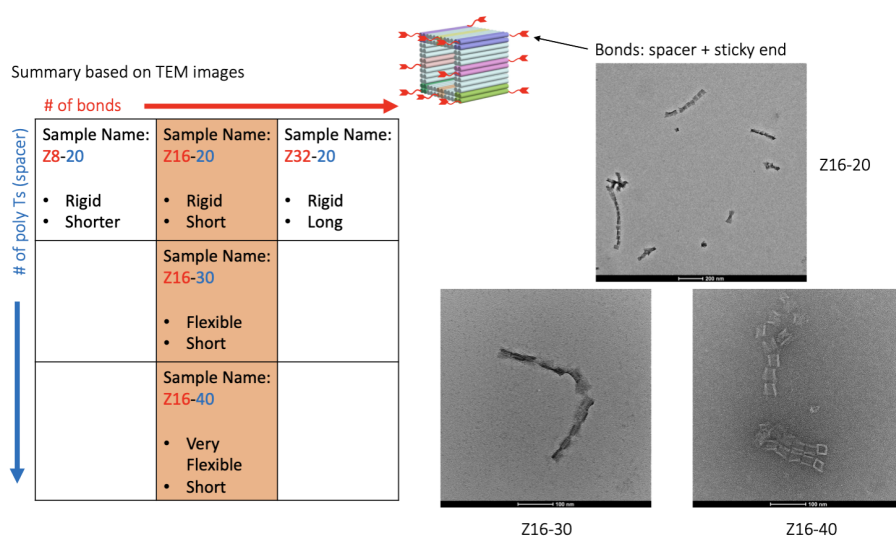

Figure 5: Summary of TEM imaging results for 1D HSo *Z16* chains, based on changing poly-T spacer length (*Z16-20*, *Z16-30* and *Z16-40*) of ssDNA linkers.

difference between between *Z16-30* & *Z16-40* in terms of rigidity is slight, and hard to distinguish from TEM images. This, however, is understandable. Because HSo are cubes after all, their ability to slide next to each other is greatly reduced compared to spherical units. A 20 poly-T spacer *ssDNA* linker has 28 bases protruding form the HSo (we assume that the staple part does not contribute to the protrusion as it is should in principle be within the origami structure). As a rough estimate, the length of a single base is 0.57 nm (we took the average value between what is proposed as the correct value in the references).[69, 70] Therefore the fully extended, protruding length of the *ssDNA* linker with 20 poly-T spacers is about 16nm. When *type-A* and *type-B* HSos with 20 poly-T spacer linkers bond, this means that the maximum face-to-face distance between them will be 26nm. This will not allow for cubic units to slide next to each other, and therefore we see *Z16-20* as rather rigid chains. *Z16-30* & *Z16-40* HSos, however, have potentially 11 and 22 nm extra room for cubes to slide next to each other, respectively. Once sliding is possible, linker length does not play a role, and the rigidity of 1D HSo chains comes down to the properties, their number and grouping of *ssDNA*.

3.2.1.2 SASX on 1D HSo Chains In addition to TEM imaging, we performed Small-angle X-ray Scattering (SAXS) measurements on our samples, using the NSLS-II facility at BNL. Scattering experiments, such as SAXS, are uncommon for measurements of 1D origami structures such as ours. Lets elaborate on the reasons for this. Scattering experiments are best suited for probing for structure of ordered, 3D lattices. In such a case the Fourier modes contributing to the intensity spectrum obtained from the
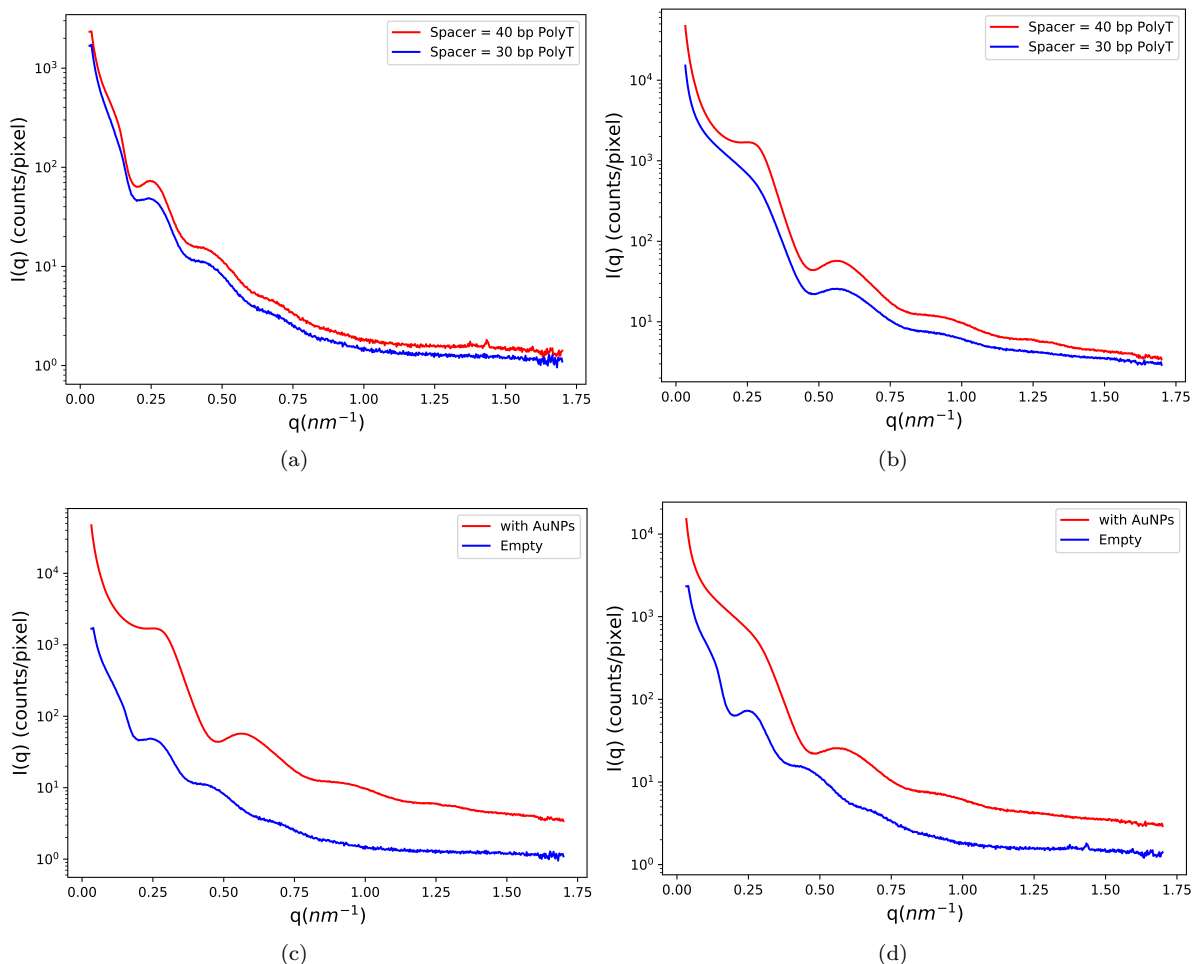

Figure 6: Intensity spectra form SASX experiments. Subplot (a) superimposes *Z16-30* and *Z16-40* 1D HSo chains without AuNPs attached to them. Subplot (b) superimposes a *Z16-30* and *Z16-40* 1D HSo chains with AuNPs attached to them. Subplot (c) shows a comparisons between the scattering profiles of *Z16-30* 1D HSo chains with and without AuNPs. Subplot (d) shows a comparisons between the scattering profiles of *Z16-40* 1D HSo chains with and without AuNPs. Form factors of AuNPs have been subtracted in for all scattering profiles.

scattered beam, will correspond to a (x,y,z)-positioned feature of the lattice structure, i.e. a feature at a particular spatial point. For 2D lattices, this Fourier space to real space projection will correspond to features on a line instead at a particular point. The features lying on this line are indistinguishable from each other, without particular theoretical assumptions for the system that is being measured upon. For 1D lattices, i.e. 1D chains, each point in Fourier space corresponds to a whole 2D plane of real space coordinates. Models for dealing with this ambiguity are only available for simple rods, or worm-like chain polymers. In practical terms, in a suspension of 1D HSo chains, it would be impossible to distinguish whether the contributions to a peak of a intensity spectrum are coming form, for example, multiples of lattice constant spacing within a single chain, or "cross-talk" contributions form nearby chains. Second point of concern for 1D lattices in SAXS experiments is that the signal would simply be to weak. Ordered, 3D lattice structures have repeated motives in three dimensions, and therefore, taking again the example of lattice constant spacing, there would be plenty of instances in the lattice where this spacing is repeated, and therefore plenty of contributions to the intensity of the scattered spectrum, without the structures having to be particularly large. For 1D lattices, such as our 1D HSo chains, that have repeating motifs only along one axis, we are limited by chain length. As such the signal coming from the origami chains would be too weak to be measured.

In spite of these shortcomings we opted to do SASX measurements. Spurred by scientific curiosity, we nonetheless had good reasoning and valid expectations from such experiments. The ambiguity stemming from back-propagation from Fourier space to real space for 1D lattices, we outlined above, can be mostly amended if one uses a very low concentration sample. Given that quantities extracted form scattering are average quantities, a low concentration sample would imply a low probability of the aforementioned "cross-talk", and therefore on average should not really affect our results significantly. The second issue we outlined above could not be amended as such, and extracting polymeric properties such as the radius of gyration was not an option for chains of length distribution such as we were getting for *Z16* HSo chains. However, there was a way to estimate the equilibrium distance between the HSos within a 1D chain conformation, and to probe whether we would be able to see a difference in this distance based on poly-T spacer length. Namely, if one was to bind 10 nm gold nanoparticles (AuNPs) to the HSo, as depicted in Fig.2(e), by examining the scattering off of the NPs, we could incur about the microstructure of 1D HSo chains. AuNPs are a particularly good choice for scattering, with a well known and pronounced scattering profile and form factor. The first peak in the intensity spectrum, that we were able to distinguish from the form factor of the NPs, would be the measure of the average distance between the nearest neighbour NPs. Given that we know the dimensions of the HSo we could use this quantity to extrapolate what is the equilibrium length of inter HSo links and therefore the average distance between the origami.

Looking at Fig.6, we could not not differentiate 1D HSo *Z16-30* and *Z16-40* chains one from another. Actually, after subtracting the AuNP form factor, very little information remains in the scattering profiles. Luckily in most cases we could still discern the first scattering profile peak, which is the quantity that is supposed to correspond to the lattice constant of out 1D HSo chains, in the case when there are no AuNPs attached to the chains, or the average space between nearest neighbour AuNPs, when they are attached to the chains. Surprisingly, even though there is a difference in signal intensity between the chains with AuNP and empty chains, we could still discern some features from the empty samples. The first peak in all of the scattering profiles occurs around $q = 0.27$, corresponding to a distance of $21 - 23$ nm. If one takes this as a representative value of the nearest neighbour AuNPs within a single chain, then we can infer that the average distance between HSo belonging to the same chain is around 15 nm for both *Z16-30* and *Z16-40* chains.

3.2.1.3   Imaging of 1D HSo Chains using AFM   Experimental measurements of equilibrium polymeric properties, a step of paramount importance in our attempts to bridge theoretical understanding, computational modelling and experimental realisation of 1D HSo based chains with MNPs, proved to be difficult in much more subtle ways than anticipated. Driven by wanting to obtain equilibrium measures that characterise 1D HSo chains, we strived to use measurement methods that are invasive as little as possible, in order to maintain the quantities we extract representative of equilibrium state and statistically significant. In light of this, we dedicated most of our measurement time to liquid AFM imaging, shown in Fig.7. In principle, it is desirable to do measurements of polymeric properties in liquid, because even though there are definitely not unadulterated filament conformations, they are much more representative then dry samples would be. In particular liquid AFM measurements should be much more representative

than TEM measurements. This is why TEM is preferably used for imaging purposes rather than feature extraction. For a detailed description of the sample preparation for liquid AFM measurements, we refer the reader to Appendix C. We highlight here that as a part of sample preparation, a certain concentration of magnesium ions is added to the MICA surface (see Appendix C), on to which sample of 1D HSo chains has been deposited. This is done in order to introduce electrostatic interactions between the surface on to which the suspension containing a sample of 1D HSo chains is deposited and the sample itself. These induced electrostatic interactions in principle slowly pin the chains in she sample on to the MICA surface. However, magnesium ions also screen much of the electrostatic interactions between the HSo casings, usually present in DNA based systems. This means that the *ssDNA* linkers might be
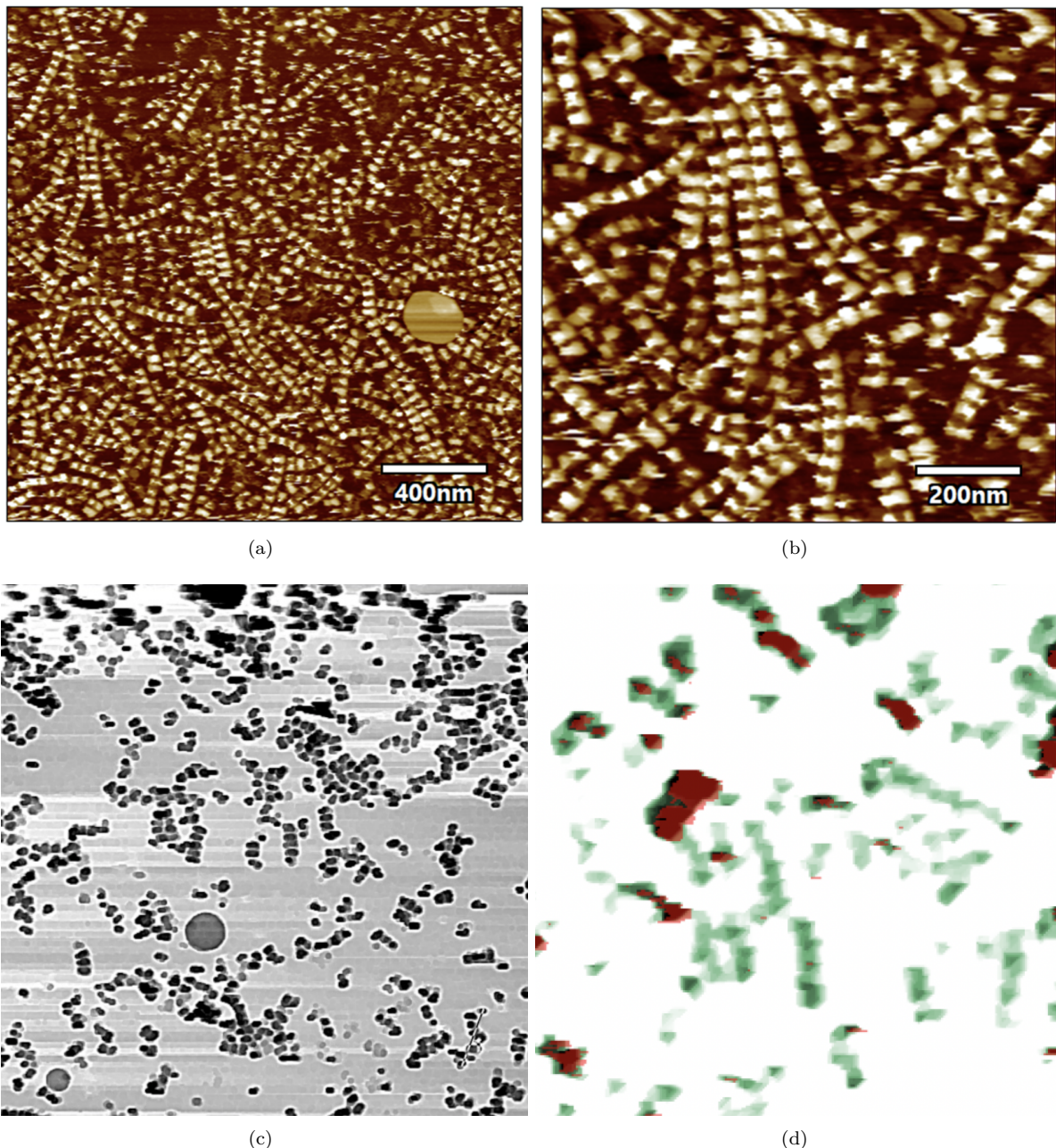

Figure 7: Pictures taken using liquid AFM. Subplot (a) depicts $Z32-20$ 1D HSo chains for scan size $2\mu m$. Subplot (b) shows a $Z32-20$ 1D HSo chains for scan size $1\mu m$. Subplot (c) shows a $Z16-40$ 1D HSo chains for scan size $2\mu m$. Subplot (d) shows a $Z16-40$ 1D HSo chains for scan size $1\mu m$, at half of magnesium concentration than used for subfigures (a)-(c). For details on sample preparation see Appendix C. Red masks denote structures taller than $36nm$ indicating aggregation perpendicular to MICA surface

interpreted as a bit more flexible then they actually are. The biggest problem that we faced when doing Liquid AFM measurements is the fact that our 1D HSo chains form regions of large concentration, as can be seen in Fig.7(a) and Fig.7(b). When deposited on to the MICA surface, they look like they are pushing on to each other, many of them overlap, and it is in general hard to discern where does one chain end and another chain starts. This is an issue because in this situation, we can forget about the notion of obtaining equilibrium polymeric properties from regions where 1D HSo chains basically aggregated. This is not data that can be used to extract equilibrium properties. By reducing magnesium concentration twofold, we did manage to reduce the degree of aggregation, but caused problems in imaging since sample was not pined to the MICA surface and would move during the measurement, as can be seen from the decreased resolution in Fig.7(d). We were however able to obtain rather high resolutions images of our structures, with the magnesium concentration, as described in Appendix C and with some post-processing, we were able to obtain rather clear images, as depicted for $Z16 - 40$ 1D HSo chains in Fig.7(c).

During our stay at CUNY and BNL, we didnt manage to avoid this aggregation, and therefore did not manage to extract equilibrium polymeric properties. However we recognised several possible mechanism that might explain it. There might be some residual central attraction forces that cause the aggregation, or it the explanation might lie in a depletion interaction due to the size distribution of the constituents in the suspension. Using a polylysin coating on the MICA surface instead of magnesium might alleviate much of these problems, but we did not manage to explore this option far enough.

4   Computational Modelling of 1D Hollow Square Origami Chains

In our research proposal we stated our intent as: "We plan to, in close collaboration with our experimental partners, provide a theoretical and computational modelling background to the synthesis, provide desired physical properties, based on our previous studies of MF systems and refine our theoretical models according to the new information." In Section 2, based on theoretical and computational considerations, we have stated explicit design criteria, as determined based on the results of simulations done with the generalised crosslinking model presented in Appendix A. This model contains all fundamental mechanisms and forces in play (excluding electrostatic interactions) and as such, can in principle be appropriated to fully represent 1D HSo chains with magnetic NPs. However, in order to do so, one has to be able to establish appropriate parameter scaling laws, so that model parameters can be appropriately tuned. This, rather unsurprisingly is a rather involved task that has to be performed in stages. General idea of how we would approach this modelling and appropriation task, in an ideal situation (where one can experimentally measure sample properties without restrictions), naturally starts with us firstly obtaining a comprehensive set of polymeric properties. We would then try to reproduce these measured quantities, with a computational model. This computational model would have to be explicit, i.e. have to fully and accurately encompass and represent the features of 1D HSo chains with and without magnetic NPs. By explicit computational modelling, which is meant to differentiate this new model from the generalised crosslinking model we introduced earlier, we mean two things. A 1D HSo chain with MNPs is different from a typical representation of a nanoscopic magnetic filament on account of firstly, having cubic steric casings for the MNPs (HSo), instead of just spherical magnetic monomers and secondly, having groupings of *ssDNA* linkers instead of a more typical "polymeric" backbone. Because of this, an bond-specific computational model would have to account for the excluded volume effects introduced by the steric casings and model the dynamics of the individual *ssDNA* linkers explicitly, rather than using an effective potential linker approach. We want to stress that all of the aforementioned and further described features, are implemented as a part of both the bond-specific and generalised crosslinking computational models. No further coding is necessary in order to access any functionality mentioned.

4.1   Bond-specific model of 1D HSo chains

A schematic depiction, along with short description of key elements of this bond-specific model can be seen in Fig.8. For further detail about the bond-specific model of 1D HSo chains, refer to Appendix B. The model was realized in the following way. We create a linear confirmation of particles, we will refer to as center-of-mass (CM) monomers, for each of which we create a cuboid shell of virtual sites. We distinguish these particles that make out the cuboid shell around the real particles as virtual, because they are excluded from equations of motion calculations, since they have a fixed position relative to the CM particle they are assigned to. Note that with face of the cuboid shell, we are talking about

The soft core steric interaction between the beads is modelled with a Weeks-Chandler-Anderson pair potential (WCA):
$$U_{WCA}(r) = \begin{cases} U_{LJ}(r) \quad - \quad U_{LJ}(r_{cut}), & r < r_{cut} \\ 0, & r \geq r_{cut} \end{cases}$$

Sticky ends interact with each other via the standard LJ-potential:
$$U_{LJ}(r) = 4\epsilon \left\{ (\sigma/r)^{12} - (\sigma/r)^6 \right\}$$

HSo excluded volume modelled with virtual sites (red) with permanent positions w.r.t a real particle (black). Steric repulsion between the virtual attracted to the same particle is excluded.

The constraining effects of the cross-linkers that bond any pair of neighbouring particles are represented by a FENE bond.
$$V(r) = -\frac{1}{2} K \Delta r_{max}^2 \ln\left[1 - \left(\frac{r - r_0}{\Delta r_{max}}\right)^2 \right]$$

Cross-linker rigidity and the orientation coupling between the particles is realised via an isotropic bonding pair potential, as depicted in Fig.1(c):
$$U_{bend}(\phi) = \frac{K_b}{2}(\phi - \phi_0)^2$$

We achieve sticky end bonding by using a harmonic bonds that force the sticky ends to a position that corresponds to the minimum of the attractive LJ-potential. This bond is subsequently removed.
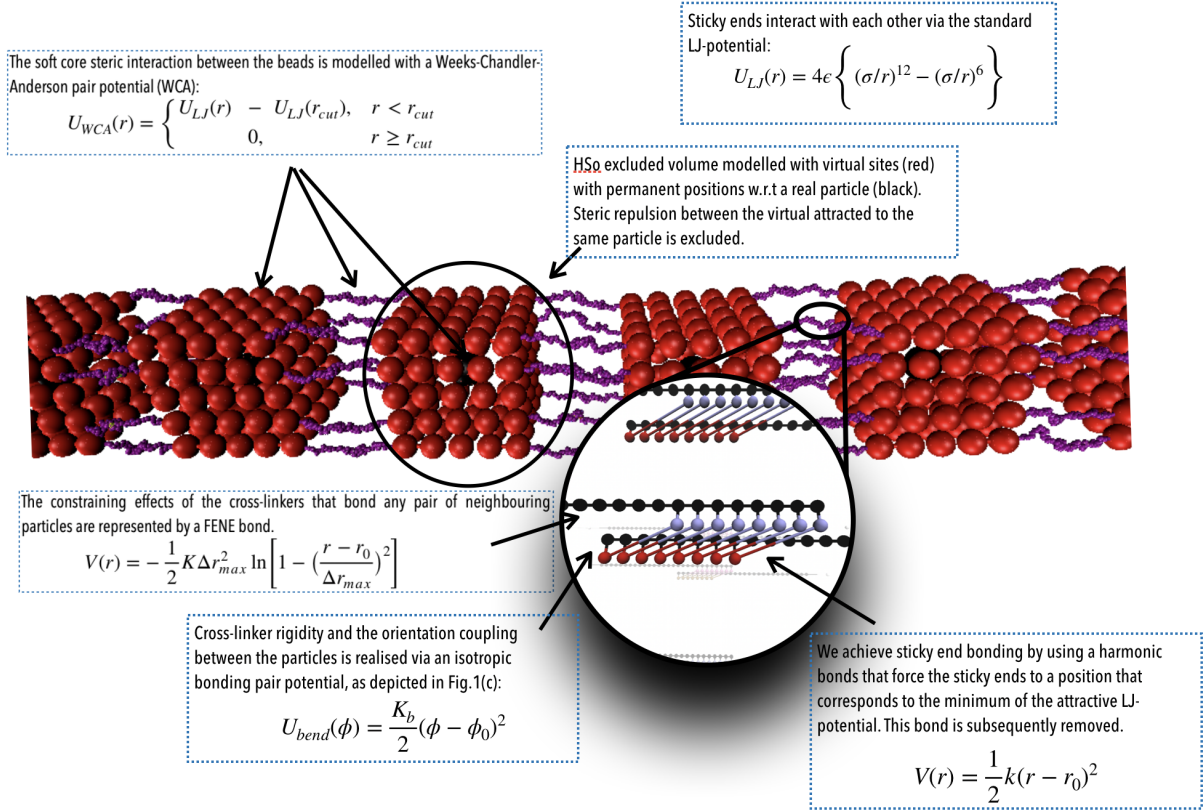$$V(r) = \frac{1}{2}k(r - r_0)^2$$

Figure 8: Schematic depiction of an bond-specific model of 1D HSo Chains

the sides of the cuboid shell pointing along the axis established by the conformation of CM particles. As suggested by the naming, CM particles are positioned at the center-of-mass of their cuboid shells, respectively. Each shell of virtual sites, together with the CM particle they are assigned to, make out a single HSo. Note that the CM particles, in addition to carrying the mass of a HSo, can easily be made to represent both NPs and MNPs. For magnetic systems, we can account for both ferromagnetic and super-paramagnetic MNPs. If the CM particles are set to be super-paramagnetic, they use the same model of magnetisation as the generalised crosslinking computational model (see Appendix A). In this way we supplement the concepts already introduced with the generalised crosslinking computational model, with excluded volume effect due to the origami. Binding vertices that allow HSos to assemble in to 1D chains are realised by attaching explicit *ssDNA* linkers to the virtual shells of CM particles (to the aforementioned faces of the cuboid shell), in a particular grouping. By explicit *ssDNA* linkers, we imply that each base in a *ssDNA* strand corresponds to a massive particle in or simulations (excluding the staple part), we will henceforth refer to *ssDNA*-base particle, each of which is linked center-to-center by FENE bonds (see Eq.3 in Appendix A).

Furthermore, between each three *ssDNA*-base particle set, there is a three particle bending potential, which allows us to mimic *ssDNA* polymeric properties (see Eq.4 in Appendix A). Specific for *ssDNA*-base particles that correspond to *ssDNA* stick ends (last eight particles of each *ssDNA* linker), as is suggested in the insert of Fig.8, each of them has an additional particle attached to it, again center-to-center via FENE bonds, that we will refer to as sticky particles. Similarly as for *ssDNA*-base particle, in addition to the FENE bonds, there are three particle bending potentials. However these bending potentials are tuned so they maintain a 90° angle between the sticky particles and the *ssDNA*-base particles. Sticky particles interact between each other via a LJ-potential (see Eq.2 in Appendix A). At the anchoring point where a *ssDNA* linker is attached to a virtual shell particles, there is a bending potential, tuned to keep the *ssDNA* linker protruding outward from the HSo, perpendicular to the face of the cuboid shell. This is necessary, given that FENE bonds will allow the linker to freely rotate around the virtual particle it is attached to (excluding steric forces, Eq.1 in Appendix A). In this way we also ensure more efficient momentum transfer form the DNA links to the Hollow cubes. Given that we had no interested in simulating assembly of HSo, but were interested in the properties of already assembled 1D chain HSo

structures and how do these properties scale with *ssDNA* linker number and poly-T spacer length, we used additional harmonic bonds between sticky particles belonging to complementary *ssDNA* sticky ends, as depicted in the insert of Fig.8, to force them to quickly bond (see Eq.10 in Appendix B). In this context, bonding means that the sticky particles belonging to complementary *ssDNA* sticky ends are positioned as is required in order the minimum of their respective interaction potentials (LJ-potentials) be reached. In this way, in only a short integration run we can "bond" the HSo, and proceed to thermodynamically equilibriate the structure.

4.2   Simulation Protocol and Results

We performed extensive MD simulations in the canonical ensemble. Just as we decided to firstly tackle the synthesis of a backbone which is ready to be impregnated with MNPs after the fact, we decided to investigate the properties of a 1D chain of HSo, without MNPs. Once we managed to obtain a good correspondence between the measures obtained from experimental measurements and simulation efforts we would proceed to investigate the polymeric and magnetic properties of 1D chains of HSo with MNPs, at different values dimensionless applied filed H and saturation magnetisation of the MNPs $\vec{\mu}_{max}$. During the time relevant to this research proposal and report, we only managed to partially tackle the non-magnetic 1D HSo chain case. The simulations were done using ESPResSo.[71] Simulation of the background fluid was done using Langevin Dynamics (LD).[72] There are multiple steps to a single simulation run. After initialising the particles and interactions in the system, we place additional harmonic bonds between complementary sticky particles, as was indicated above. The positions of the CM particles are initially fixed (therefore also the positions of virtual shell particles are initially fixed), in order to allow the *ssDNA* linkers to bond and relax w.r.t thermal fluctuations. We start our first relaxation cycle with a rather small timestep of 0.0001, and integrate for 30 000 timesteps. Then we increase the timestep tenfold to 0.001 and integrate for another 100 000 timesteps. After this, we remove the harmonic bonds between the complementary sticky particles, and remove the constraint that positions of the CM particles are fixed. The we perform a final relaxation cycle, integrating for 2 000 000 timesteps. After this we start the measurement integration loop, where we integrate for 10 500 000 timesteps, recording data snapshots every 30 000 integrations. All results presented are made based on average of four independent initial configuration runs. Were there super-paramagnetic MNPs embedded in to the 1D HSo chains, we would run an additional relaxation cycle for 10^7 integration steps, after which we would switch on an external magnetic field $\vec{H}$, and start recording data. In this case, initial orientations of MFs in our simulations would be uniformly distributed on a surface of a sphere. We would use an iterative magnetisation procedure, described with Eq.(8). Computationally, after every integration of Eq.(9), we would reevaluate the total magnetic field $\vec{H}_{tot}$, and based the approach we describe in Appendix 5, reassign new values of dipole moments to the magnetic monomers in the system.

Experimentally, we have recognized two variables to be adequately tuned. As explained in Section 2, the variables in question are: number of *ssDNA* inter-cage linkers and the length of such linkers (no. of spacer polyT). These two variables are a part of a larger relationship between the chain rigidity and net bonding energy. However we wanted to investigate this relationship to a degree that supersedes intuitive notion of the cause and effect w.r.t the aforementioned parameters. Computationally, one can easily change both the poly-T length and number of *ssDNA* linkers, and run a batch of parallel simulations across the range of parameters of interest. By comparing the value of radius of gyration of 1D HSo chains, as a function of *ssDNA* linker poly-T spacer length and/or number of *ssDNA* linker, one can estimate the relationships between these parameters quantitatively rather than only qualitatively. In principle, the relationship between chain stiffens and number of *ssDNA* linkers can be estimated as simply as a linear interpolation. Furthermore, it is disadvantageous to model explicitly a large number of *ssDNA* linkers. A relationship between stiffens and number of *ssDNA* linkers allows one to use single linker effective representation of many *ssDNA* linkers, mostly for resource management. Furthermore, one would eventually want to transition from bond-specific representations to more general and "coarse-grained" representations, in order to highlight the physics behind rather than highlight structural features. In this case this would mean that one uses effective potential representation of the *ssDNA* linkers, in order to effectively replace the bond-specific model with the aforementioned generalised crosslinking computational model, which if done properly, gives a general model without a loss in accuracy for the specific system we are tackling.

We want to stress the importance of resource management in these simulations. Already for a 1D

HSo chain consisting of 10 CM particles, with cubic $5\sigma \times 5\sigma \times 5\sigma$ virtual particle shell, and single $ssDNA$ linker per corner with 20 poly-T spacers (four linkers per HSo face), simulations last up to 3 days. If we want to double the number of $ssDNA$ linkers per face of HSo, we have to deal with either running longer simulations or trading statistical significance of our results. This should put i perspective the importance of finding appropriate generalised crosslinking representations and models for such systems. Due to time and resource constraints, during our appointment in CUNY and BNL, we only managed to obtain statistically significant results for the Square of the Radius of Gyration R_g^2 of 1D HSo chains, in two cases. Namely, in light of our interest in the relationship between chain stiffens and number of $ssDNA$ linkers, we considered the change in R_g^2 for 1D HSo chains consisting of 10 CM particles, with cubic $5\sigma \times 5\sigma \times 5\sigma$ virtual particle shell, with either a single $ssDNA$ linker or two $ssDNA$ linkers per HSo face corner with 20 poly-T spacers. We normalise R_g^2 by the factor $(d*(N-1)/2)^2$, where d is the CM particle center-to-center distance and N is the number of CM particles. Note that the maximum value for $R_g^2 = 0.368$ is determined as the normalized R_g^2 for a static rod with equivalent d and N. For the case of a single $ssDNA$ linker per HSo face corner, we obtained $R_g^2 = 0.174$, which is roughly 45% of the maximum possible value. For two $ssDNA$ linkers per HSo face corner, we obtained $R_g^2 = 0.203$, which is an increase of roughly 8% compared to the case with a single $ssDNA$ linker pr HSo face corner, relative to the maximum value possible. Based on expectations we have from the experimental imaging of these systems, we expect that adding a third and forth $ssDNA$ linker per HSO face corner will further increase the R_g^2, but only slightly. In any case, even though the R_g^2 values we obtained are higher than what one would observe for a real polymer (in our units this value corresponds to roughly $R_g^2 = 1.12$), the difference is not prohibiting. Given the amount of excluded volume stemming from the HSo, reaching real polymer was never an option, but we can still conclude that these systems should have sufficient flexibility.

We will wrap up the discussion presented in this section, with some insight we obtained just from looking at the individual trajectory files from ours simulations. Visual inspection of the trajectories reveals that the 1D HSo chains do not really coil, a behaviour which is characteristic of any real polymer, of even MFs in weak magnetic fields. The reason for this was a bit unexpected but is rather intuitive. Bonds between complementary HSo types, realised by means of $ssDNA$ linkers, are entropy sinkholes. The number of $ssDNA$ linkers and particles within each of them ($ssDNA$-base particles and sticky ends in terms of we used for simulations), means that there are lots of conformations for 1d HSo chains to explore. With a Langevin thermostat, really most of the entropy goes to reduction of the end-to-end distance of the $ssDNA$ linkers, and once they reach a thermodynamically stable state, a signle HSo mostly moves around in a spherical volume with a diameter not much larger then $1.5*d$, where d is the long diagonal of a single HSo, centered at the initial position of the HSo in question. There is not reason for the origami to coil because entropy induced momentum is transfer very indirectly to them. If it was a "hinge", where each monomer was connected to the next one via a single swiveling point of contact, i.e. having HSo connected corner to corner instead of face to face, we could expect coiling, but like this, DNA linkers simply act like shock absorbers. However, this underlines the possibility that these systems could have significant benefits in hydrodynamic environments, and be much more structurally sound under shear stress for example, compared to a "hinge" connected system.

Furthermore, if we want to compare polymeric properties extracted from AFM measurements for example, to equilibrium properties extracted form MD simulations we have two choices. We could make a theoretical model assumption based on, for example, the scaling of end-to-end distance and monomer number, in order to extrapolate a 3D version of whatever 2D polymeric properly we are extracting form experimental measurements (once you pin the sample to the MICA surface for an AFM measurement, it effectively becomes a 2D system). Alternatively, one could consider a planar projection of the 3D system and than make an estimate of the polymeric properties. Ideally, if computational resource allow, one would also like to introduce electrostatic charges in to the system, in order to attempt to closely mimic also the environment that 1D HSo chains are in during an experimental measurement, although this would probably only be possible once one migrates to an generalised crosslinking computational representation of the chains, in particular, replaces explicit $ssDNA$ linkers with effective potential representations.

5 Appendix A

In the generalised crosslinking computational model, we consider MFs as consisting of mono-disperse monomers, modeled as identical spherical particles with a characteristic reduced diameter $\sigma = 1$ and reduced mass $m = 1$. In this model monomers can be non-magnetic, ferromagnetic or super-paramagnetic. The steric interaction between the particles is given by the Weeks-Chandler-Andersen pair potential (WCA),[73]:

$$U_{WCA}(r) = \begin{cases} U_{LJ}(r) - U_{LJ}(r_{cut}), & r < r_{cut} \\ 0, & r \geq r_{cut} \end{cases} \tag{1}$$

where $U_{LJ}(r)$ is the conventional Lennard-Jones potential:

$$U_{LJ}(r) = 4\epsilon \left\{ (\sigma/r)^{12} - (\sigma/r)^6 \right\} \tag{2}$$

and the cutoff value is $r_{cut} = 2^{1/6}\sigma$. Parameter ϵ defines the energy scale of the repulsion when the inter-particle distance r decreases. As suggested Section 2, and depicted in Fig. 1 we explore two crosslinking mechanisms between the monomers, which we refer to as either plan and constrained crosslinking, respectively. By plain crosslinking, it is to be understood that neighbouring monomers of an MF are bonded center-to-center via the $FENE$ potential, given by:

$$U_{FENE}(r) = \frac{-K_f r_f^2}{2} \ln \left\{ 1 - \left(\frac{r}{r_f} \right)^2 \right\}, \tag{3}$$

where $r_f = 2\sigma$ and $K_f = 2.5$ are the maximum extension and the rigidity of a FENE bond respectively. In this way, we ensure a close contact between the monomers, without restricting their rotations. For the constrained crosslinking mechanism, in addition to the center-to-center $FENE$ potential between the monomers, we add an isotropic bonding pair potential between first-nearest neighbors:

$$U_{bend}(\phi) = \frac{K_b}{2} (\phi - \phi_0)^2, \tag{4}$$

where ϕ is the angle between the vectors spanning from particle i to its nearest neighbour particle pair $(i-1, i+1)$, $i \in [2, N-1]$. $K_b = 3.2$ is the bending constant, while $\phi_0 = \pi$ is the equilibrium bond angle. In this was we achieve a backbone with significant stiffness against bending.

If the monomers are ferromagnetic, they carry point magnetic dipole moments located at their centers, denoted by $\vec{\mu}$. Long-range magnetic inter-particle interactions are accounted for via the dipole-dipole pair potential:

$$U_{dd}(\vec{r_{ij}}, \vec{\mu_i}, \vec{\mu_j}) = \frac{\vec{\mu_i} \cdot \vec{\mu_j}}{r_{ij}^3} - \frac{3(\vec{\mu_i} \cdot \vec{r_{ij}})(\vec{\mu_j} \cdot \vec{r_{ij}})}{r_{ij}^5}, \tag{5}$$

where $r_{ij} = |\vec{r_{ij}}|$, and $\vec{r_{ij}} = \vec{r_i} - \vec{r_j}$ is the displacement vector connecting the centers of particles i and j with dipole moments $\vec{\mu_i}$ and $\vec{\mu_j}$, respectively. Furthermore, we consider Zeeman interactions coming from the presence of an external magnetic field $\vec{H}$:

$$U_H(\vec{H}, \vec{\mu_i}) = -\sum_{i=0}^{N} \vec{H} \cdot \vec{\mu_i}. \tag{6}$$

If the monomers are super-paramagnetic, one needs to accurately calculate the total field $\vec{H}_{tot}$ in each point of the system. The total magnetic field is the sum of $\vec{H}$ and the dipole field $\vec{H}_d$. The latter field, created by monomer j, at position $\vec{r_0}$ is given by:

$$\vec{H}_d = \frac{3\vec{r_{0j}} \cdot \vec{\mu_j}}{r_{0j}^5} \vec{r_{0j}} - \frac{\vec{\mu_j}}{r_{0j}^3}. \tag{7}$$

The study of the response of a filament to fields of arbitrary strength requires to one define the dipole moment, $\vec{\mu_i^s}$, of an i-th super-paramagnetic particle at a given temperature T, as:

$$\vec{\mu_i^s} = \mu_{max} L \left(\frac{\mu_{max} |\vec{H}_{tot}|}{k_B T} \right) \frac{\vec{H}_{tot}}{H_{tot}}, \tag{8}$$

where $\mu_{max} = |\vec{\mu}_{max}|$ denotes the modulus of the maximal magnetic moment of the particle $\vec{\mu}_{max}$. Here, k_B is the Boltzmann constant and $L(\alpha)$ is the Langevin function:

$$L(\alpha) = \coth(\alpha) - \frac{1}{\alpha}. \tag{9}$$

This approach allows us to consider nonlinear magnetisation effects. The long range magnetic interaction and the Zeeman coupling for super-paramagnetic particles are accounted for just as they are for ferromagnetic monomers, see Eqs. (5) and (6), respectively. Because of the fact that we are interested in the competition between the dipole-dipole interaction entropy, we have chosen to set the energy scale to be measured in units of thermal energy, $k_b T = \epsilon = 1$,

6   Appendix B

Here we present in detail the bond-specific 1D chin HSo bead-spring model, introduced in Section 4 and depicted in some detail in Fig.8. Each particle in the system (we distinguished CM particles, virtual shell particles, *ssDNA*-base particles and sticky particles) is modeled as a spherical bead with a characteristic diameter σ. The steric interaction between the particles is given by Eq.1, with a cutoff value of $r_{cut} = 2^{1/6}\sigma$. As previously mentioned, CM particles can be set to represent MNPs, either ferro- or super-paramagnetic ones. If the CM particles are ferromagnetic MNPs, we introduce point magnetic dipole moments $\vec{\mu}$ of fixed length $|\vec{\mu}| = \mu$, located at particle centers. Long-range magnetic inter-particle interactions are accounted for via Eq.5. Zeeman interactions coming from the presence of an external magnetic field $\vec{H}$ are accounted via Eq.6.

If however the CM particles are super-paramagnetic MNPs, just as was explained in Appendix A, in order to consider nonlinear magnetisation effects, one needs to accurately calculate the total field $\vec{H}_{tot}$ in each point of the system. The total magnetic field is the sum of $\vec{H}$ and the dipole field $\vec{H}_d$. The latter field, created by CM particle j, at position $\vec{r}_0$ is given by Eq.7. The study of the response of a filament to fields of arbitrary strength requires to one define the dipole moment, $\vec{\mu}_i^s$, of an i-th super-paramagnetic CM particle at a given temperature T, as given in Eq.8. The long range magnetic interaction and the Zeeman coupling for super-paramagnetic particles are accounted for just as they are for ferromagnetic monomers, see Eqs. (5) and (6), respectively.

Bond-specific modelling of the *ssDNA* linkers, as previously explained, entails that each *ssDNA* base is modeled as a massive particle. The basic connectivity mechanism between the particles representing the *ssDNA* linkers, encompassing the connections between the *ssDNA*-base particles, between sticky particles and the *ssDNA*-base particles, and finally between the virtual shell particles and the *ssDNA*-base particles are finitely extensible nonlinear elastic potentials ($FENE$), given in Eq. 3. Continuing on what was explained in Section 4, by adding isotropic bonding pair potentials between first-nearest *ssDNA* particle (*ssDNA*-base particles, sticky particles) neighbors,, given in Eq. 4, we were able to make bond-specific representations of *ssDNA* linkers with realistic *ssDNA* polymeric properties. As explained in Section 4, we used classical harmonic potentials to force the sticky particles in the minima of their respective LJ-potentials, in order to form *ssDNA* bonds quickly and efficiently. The classical harmonic potential has the form:

$$U_{har}(\phi) = \frac{k_h}{2}(r - r_0)^2 \tag{10}$$

with r_0 denoting the equilibrium length and k_h denoting the attraction strength. It is a symmetric interaction between two particles.

The length scale in our systems is determined by setting the diameter of the steric potential given in Eq. (1). For CM particles, *ssDNA*-base particles $\sigma = 1$, sticky particles $\sigma = 0.35$ while for virtual shell particles $\sigma = 8$. The energy scale is determined by the choice of the reduced temperature $k_b T = 1$. The strength of the steric interaction potentials between all types of particles in our simulations (inclusive of virtual shell particles, *ssDNA*-base particles and sticky particles, where steric interactions between virtual shell particles associated to the same CM particle are excluded) to $\epsilon = 1$. Therefore, the energy in our simulations is measured in units of $k_B T$. The reduced characteristic mass of the *ssDNA* particles (*ssDNA*-base particles and sticky particles) is $m = 1$. The mass of CM particles was determined by counting the virtual particle number in the cuboid shell, summing their masses as if each of the virtual

shell particles related to the CM particle in questions had $m = 1$, and divided the summed mass by 10. Using this mass, we reset the tensor of inertia for each CM particle. In this way we set the relative mass of HSo compared to unit mass that each of the particles that compose the *ssDNA* linkers carry.

Given that we are only interested in equilibrium properties of 1D HSo chains, the actual particle mass is not relevant, but tensor of inertia of CM particles must be set to represent the fact that they carry a shell of virtual particles. The LJ-interaction between the sticky particles is set with the following reduced parameters: $\epsilon = 10$, $\sigma = 0.35$ and $r_{cut} = 0.875$. Connections in between *ssDNA*-base particles, between *ssDNA*-base and sticky particles, and connections between *ssDNA*-base and virtual shell particles (potential given in Eq. (3)), have $K_f = 10$, with the maximum extension of the the FENE bond $r_f = 2\sigma$. The bending constant K_b of the harmonic angle dependent potential given in Eq. (4), between each three *ssDNA*-base particle set is set to $K_b = 0.7$, with the equilibrium bond angle $\phi_0 = 0$. The bending constant K_b of the bending potential between each set consisting of two neighbouring *ssDNA*-base particles and a sticky end particle attached to one of the *ssDNA*-base particles, is $K_b = 30$, with the equilibrium bond angle $\phi_0 = \pi/2$. Bending potential between the virtual shell anchors and *ssDNA* linkers have the bending constant $K_b = 100$ and equilibrium bond angle $\phi = 0$. The parameters set used for setting the harmonic potential, facilitating quick bonding between complementary *ssDNA* links is $k_h = 1$, $r_0 = 0.393$ (minimum of the LJ-potential for a sticky particles that has $\sigma = 0.35$).

7   Appendix C

7.1   Folding and purification of DNA origami

DNA origami was prepared by mixing 20 nM scaffold (M13mp18), 100 nM of each staple oligonucleotide, buffer and salts. Buffer solution contains 10 mM EDTA, 100 mM MgCl2, 100 mM Tris ($pH = 7.9$ at $20°C$). Annealing the mixed sample by PCR Thermal Cycler were introduced to fold the hollow square origami. The annealing process is that firstly heating the sample to $90°C$ from room temperature rapidly, secondly slowly cooling from $80°C$ to $61°C$ over 80 min and lastly cooling from $60°C$ to $24°C$ over 12 h. The samples were transferred with buffer to the pre-washed Amicon® Ultra-0.5 Centrifugal Filter Devices and centrifuged $(2,000 \times g, 10 \text{ min})$ to concentrate the origami with five repeats in room temperature $(24°C)$.

7.2   Measurement of the concentration of DNA origami

Measuring of the origami concentration was carried out by Thermo Scientific NanoDrop$^{\text{TM}}$ Lite Spectrophotometer. The blank measurement was firstly completed by transferring $1\mu L$ *DI* water onto the lower pedestal, following by another repeat until "Measure Sample" shown on the screen. The concentration of the origami was then obtained by loading $1\mu L$ sample onto the lower pedestal, lowering arm and pressing "Measure". It is worthwhile to note that the unit provided by the machine is $ng/\mu L$. In order to obtain the molar concentration of DNA origami (nM), the value $(ng/\mu L)$ displayed on the screen was divided by 4.125.

7.3   Synthesis of 1D chain DNA origami

In order to synthesize the 1D chain origami, we mixed two kinds of complementary DNA origamis with the molar ratio $1:1$ firstly. Then the formation of 1D chain was carried out in annealing process completed by PCR Thermal Cycler. The sample was heated up to $49°C$ in 5 min, after that, slowly cooled from $49°C$ to $22°C$ over 55 h, lastly $22°C$ to $20°C$ over 2 min.

7.4   Sample preparation for TEM

Copper mesh grids (Carbon Film 300 mesh, Copper, Ted Pella) were held for $10s$ and then glow discharged for $60s$. Diluted sample was deposited on discharged grid for 5 min. Excess sample was wicked off by filter paper. After that, the grid was washed by 5 μL distilled water twice for $15s$ each time to remove salts. Then, for samples containing DNA origami, uranyl acetate was added to the sample as a negative stain for $15s$ and wicked away. The sample was dried for 5 min prior to loading into single tilt holder of transmission electron microscope.

7.5   Sample preparation for liquid AFM

We diluted DNA origami sample in $1 \times TAE$ $12.5mM$ $MgCl2$ buffer. Then 25 L diluted sample was spotted on freshly cleaved mica and left it over ten minutes. We also tried to do measurements using poly-lysin to fix the sample, but we have unfortunately not removed enough of the coating before the measurements, to get useful results.

8   Bibliography

[1] A. C. Balazs, T. Emrick and T. P. Russell, *Science*, 2006, **314**, 1107–1110.

[2] J. Hu and S. Liu, *Macromolecules*, 2010, **43**, 8315–8330.

[3] R. Tietze, J. Zaloga, H. Unterweger, S. Lyer, R. P. Friedrich, C. Janko, M. Pöttler, S. Dürr and C. Alexiou, *Biochemical and biophysical research communications*, 2015, **468**, 463–470.

[4] Q. A. Pankhurst, N. T. K. Thanh, S. K. Jones and J. Dobson, *J. Phys. D: Appl. Phys.*, 2009, **42**, 224001.

[5] S. Odenbach, *Archive of Applied Mechanics*, 2016, **86**, 269–279.

[6] R. Dreyfus, J. Baudry, M. L. Roper, M. Fermigier, H. A. Stone and J. Bibette, *Nature*, 2005, **437**, 862–865.

[7] J. J. Benkoski, S. E. Bowles, R. L. Jones, J. F. Douglas, J. Pyun and A. Karim, *J Polym Sci, Part B: Polym Phy*, 2008, **46**, 2267–2277.

[8] A. Cēbers, *J. Phys.: Condens. Matter*, 2003, **15**, S1335.

[9] V. P. Shcherbakov and M. Winklhofer, *Phys. Rev. E*, 2004, **70**, 061803.

[10] A. Cēbers and I. Javaitis, *Phys Rev E*, 2004, **69**, 021404.

[11] A. Cēbers, *Curr Opin Colloid Interface Sci*, 2005, **10**, 167–175.

[12] M. Belovs and A. Cēbers, *Physical Review E*, 2006, **73**, 051503.

[13] A. Cēbers and T. Cīrulis, *Physical Review E*, 2007, **76**, 031504.

[14] K. Ērglis, D. Zhulenkovs, A. Sharipo and A. Cēbers, *Journal of Physics: Condensed Matter*, 2008, **20**, 204107.

[15] A. A. Kuznetsov, *Journal of Magnetism and Magnetic Materials*, 2019, **470**, 28–32.

[16] E. Gauger and H. Stark, *Phys. Rev. E*, 2006, **74**, 021907.

[17] M. Roper, R. Dreyfus, J. Baudry, M. Fermigier, J. Bibette and H. A. Stone, *Journal of Fluid Mechanics*, 2006, **554**, 167–190.

[18] M. Roper, R. Dreyfus, J. Baudry, M. Fermigier, J. Bibette and H. A. Stone, *Proceedings of the Royal Society A: Mathematical, Physical and Engineering Sciences*, 2008, **464**, 877–904.

[19] S. Huang, G. Pessot, P. Cremer, R. Weeber, C. Holm, J. Nowak, S. Odenbach, A. M. Menzel and G. K. Auernhammer, *Soft Matter*, 2016, **12**, 228–237.

[20] J. Zhao, D. Du and S. L. Biswal, *Physical Review E*, 2018, **98**, 012602.

[21] S. Kuei, B. Garza and S. L. Biswal, *Physical Review Fluids*, 2017, **2**, 104102.

[22] J. M. Dempster, P. Vázquez-Montejo and M. O. de la Cruz, *Physical Review E*, 2017, **95**, 052606.

[23] P. Vázquez-Montejo, J. M. Dempster and M. O. de la Cruz, *Physical Review Materials*, 2017, **1**, 064402.

[24] O. Philippova, A. Barabanova, V. Molchanov and A. Khokhlov, *European polymer journal*, 2011, **47**, 542–559.

[25] O. S. Pak, W. Gao, J. Wang and E. Lauga, *Soft Matter*, 2011, **7**, 8169–8181.

[26] P. A. Sánchez, E. S. Pyanzina, E. V. Novak, J. J. Cerdà, T. Sintes and S. S. Kantorovich, *Macromolecules*, 2015, **48**, 7658–7669.

[27] S. L. Biswal and A. P. Gast, *Analytical chemistry*, 2004, **76**, 6448–6455.

[28] T. Yang, T. O. Tasci, K. B. Neeves, N. Wu and D. W. Marr, *Langmuir*, 2017, **33**, 5932–5937.

[29] E. M. Furst, C. Suzuki, M. Fermigier and A. P. Gast, *Langmuir*, 1998, **14**, 7334–7336.

[30] E. M. Furst and A. P. Gast, *Phys Rev Lett*, 1999, **82**, 4130–4133.

[31] C. Goubault, P. Jop, M. Fermigier, J. Baudry, E. Bertrand and J. Bibette, *Phys. Rev. Lett.*, 2003, **91**, 260802.

[32] L. Cohen-Tannoudji, E. Bertrand, L. Bressy, C. Goubault, J. Baudry, J. Klein, J.-F. m. c. Joanny and J. Bibette, *Phys. Rev. Lett.*, 2005, **94**, 038301.

[33] H. Singh, P. E. Laibinis and T. A. Hatton, *Langmuir*, 2005, **21**, 11500–11509.

[34] H. Singh, P. E. Laibinis and T. A. Hatton, *Nano Lett*, 2005, **5**, 2149–2154.

[35] F. Martínez-Pedrero, M. Tirado-Miranda, A. Schmitt and J. Callejas-Fernández, *Phys Rev E*, 2007, **76**, 011405.

[36] B. A. Evans, A. R. Shields, R. L. Carroll, S. Washburn, M. R. Falvo and R. Superfine, *Nano Lett*, 2007, **7**, 1428–1434.

[37] Z. Zhou, G. Liu and D. Han, *ACS Nano*, 2009, **3**, 165–172.

[38] J. J. Benkoski, J. L. Breidenich, O. M. Uy, A. T. Hayes, R. M. Deacon, H. B. Land, J. M. Spicer, P. Y. Keng and J. Pyun, *J Mater Chem*, 2011, **21**, 7314–7325.

[39] H. Wang, Y. Yu, Y. Sun and Q. Chen, *Nano*, 2011, **06**, 1–17.

[40] D. Sarkar and M. Mandal, *The Journal of Physical Chemistry C*, 2012, **116**, 3227–3234.

[41] J. L. Breidenich, M. C. Wei, G. V. Clatterbaugh, J. J. Benkoski, P. Y. Keng and J. Pyun, *Soft Matter*, 2012, **8**, 5334–5341.

[42] E. Busseron, Y. Ruff, E. Moulin and N. Giuseppone, *Nanoscale*, 2013, **5**, 7098–7140.

[43] J. Byrom, P. Han, M. Savory and S. L. Biswal, *Langmuir*, 2014, **30**, 9045–9052.

[44] L. J. Hill and J. Pyun, *ACS applied materials & interfaces*, 2014, **6**, 6022–6032.

[45] M. B. Bannwarth, S. Utech, S. Ebert, D. A. Weitz, D. Crespy and K. Landfester, *ACS Nano*, 2015, **9**, 2720–2728.

[46] A. Hosseinifar, M. Shariaty-Niassar, S. Seyyed Ebrahimi and M. Moshref-Javadi, *Langmuir*, 2017, **33**, 14728–14737.

[47] Y. Xiong, Q. Chen, N. Tao, J. Ye, Y. Tang, J. Feng and X. Gu, *Nanotechnology*, 2007, **18**, 345301.

[48] Z. Zhou, G. Liu and D. Han, *ACS Nano*, 2008, **3**, 165–172.

[49] F. Zhang and C.-C. Wang, *The Journal of Physical Chemistry C*, 2008, **112**, 15151–15156.

[50] M. Ma, Q. Zhang, J. Dou, H. Zhang, D. Yin, W. Geng and Y. Zhou, *Journal of Colloid and Interface Science*, 2012, **374**, 339–344.

[51] S. H. Xu, G. T. Fei, H. M. Ouyang, Y. Zhang, P. C. Huo and L. De Zhang, *Journal of Materials Chemistry C*, 2015, **3**, 2072–2079.

[52] X. Wen, L. Gu and A. M. Bittner, *Zeitschrift für Physikalische Chemie*, 2018, **232**, 1631–1646.

[53] M. Bennet, L. Bertinetti, R. K. Neely, A. Schertel, A. Körnig, C. Flors, F. D. Müller, D. Schüler, S. Klumpp and D. Faivre, *Faraday discussions*, 2015, **181**, 71–83.

[54] É. Bereczk-Tompa, F. Vonderviszt, B. Horváth, I. Szalai and M. Pósfai, *Nanoscale*, 2017, **9**, 15062–15069.

[55] M. M. Maye, D. Nykypanchuk, M. Cuisinier, D. van der Lelie and O. Gang, *Nature Materials*, 2009, **8**, 388–391.

[56] D. Sun, A. L. Stadler, M. Gurevich, E. Palma, E. Stach, D. van der Lelie and O. Gang, *Nanoscale*, 2012, **4**, 6722.

[57] D. Sun and O. Gang, *Langmuir*, 2013, **29**, 7038–7046.

[58] Y. Zhang, F. Lu, K. G. Yager, D. van der Lelie and O. Gang, *Nature Nanotechnology*, 2013, **8**, 865–872.

[59] S. Srivastava, D. Nykypanchuk, M. Fukuto, J. D. Halverson, A. V. Tkachenko, K. G. Yager and O. Gang, *Journal of the American Chemical Society*, 2014, **136**, 8323–8332.

[60] Y. Tian, T. Wang, W. Liu, H. L. Xin, H. Li, Y. Ke, W. M. Shih and O. Gang, *Nature Nanotechnology*, 2015, **10**, 637–644.

[61] W. Liu, J. Halverson, Y. Tian, A. V. Tkachenko and O. Gang, *Nature chemistry*, 2016, **8**, 867.

[62] A. O. Ivanov and O. B. Kuznetsova, *Physical Review E*, 2001, **64**, 041405.

[63] V. A. Ivanov and J. A. Martemyanova, *Macromol Symp*, 2007, **252**, 12–23.

[64] M. M. Maye, D. Nykypanchuk, M. Cuisinier, D. van der Lelie and O. Gang, *Nature Materials*, 2009, **8**, 388–391.

[65] D. Sun, A. L. Stadler, M. Gurevich, E. Palma, E. Stach, D. van der Lelie and O. Gang, *Nanoscale*, 2012, **4**, 6722–6725.

[66] Y. Zhang, F. Lu, K. G. Yager, D. van der Lelie and O. Gang, *Nat Nano*, 2013, **8**, 865–872.

[67] Y. Tian, T. Wang, W. Liu, H. L. Xin, H. Li, Y. Ke, W. M. Shih and O. Gang, *Nature nanotechnology*, 2015, **10**, 637.

[68] Y. Tian, Y. Zhang, T. Wang, H. L. Xin, H. Li and O. Gang, *Nature Materials*, 2016, **15**, 654–661.

[69] U. Bockelmann, B. Essevaz-Roulet and F. Heslot, *Physical Review E*, 1998, **58**, 2386.

[70] Q. Chi, G. Wang and J. Jiang, *Physica A: Statistical Mechanics and its Applications*, 2013, **392**, 1072–1079.

[71] H. J. Limbach, A. Arnold, B. A. Mann and C. Holm, *Comput Phys Commun*, 2006, **174**, 704–727.

[72] M. P. Allen and D. J. Tildesley, *Computer simulation of liquids*, Oxford university press, 2017.

[73] J. D. Weeks, D. Chandler and H. C. Andersen, *The Journal of chemical physics*, 1971, **54**, 5237–5247.